Multivalent Recognition at Fluid Surfaces: The Interplay of Receptor Clustering and Superselectivity

Galina V Dubacheva, Tine Curk, Daan Frenkel, Ralf Richter

▶ **To cite this version:**

Galina V Dubacheva, Tine Curk, Daan Frenkel, Ralf Richter. Multivalent Recognition at Fluid Surfaces: The Interplay of Receptor Clustering and Superselectivity. Journal of the American Chemical Society, 2019, 141 (6), pp.2577-2588. 10.1021/jacs.8b12553 . hal-02328025

HAL Id: hal-02328025
https://hal.science/hal-02328025

Submitted on 23 Oct 2019

HAL is a multi-disciplinary open access archive for the deposit and dissemination of scientific research documents, whether they are published or not. The documents may come from teaching and research institutions in France or abroad, or from public or private research centers.

L'archive ouverte pluridisciplinaire **HAL**, est destinée au dépôt et à la diffusion de documents scientifiques de niveau recherche, publiés ou non, émanant des établissements d'enseignement et de recherche français ou étrangers, des laboratoires publics ou privés.

Multivalent recognition at fluid surfaces: the interplay of receptor clustering and superselectivity

Galina V. Dubacheva[Δ⊥‡*], Tine Curk[§‖‡], Daan Frenkel[†], and Ralf P. Richter[Δ#*]

[Δ]Biosurfaces Lab, CIC biomaGUNE, Paseo Miramon 182, 20014 Donostia - San Sebastian, Spain

[⊥]PPSM CNRS UMR8531, ENS Cachan, Université Paris-Saclay, 61 Avenue du Président Wilson, 94235 Cachan, France

[§]Institute of Physics, Chinese Academy of Sciences, Beijing 100190, People's Republic of China

[‖]Faculty of Chemistry and Chemical Engineering, University of Maribor, 2000 Maribor, Slovenia

[†]Department of Chemistry, University of Cambridge, Lensfield Road, Cambridge, CB2 1EW, United Kingdom

[#]School of Biomedical Sciences, Faculty of Biological Sciences, School of Physics and Astronomy, Faculty of Mathematics and Physical Sciences, and Astbury Centre for Structural Molecular Biology, University of Leeds, Leeds, LS2 9JT, United Kingdom

ABSTRACT: The interaction between a biological membrane and its environment is a complex process, as it involves multivalent binding between ligand/receptor pairs, which can self-organise in patches. Any description of the specific binding of biomolecules to membranes must account for the key characteristics of multivalent binding, namely its unique ability to discriminate sharply between high and low receptor densities (superselectivity), but also for the effect of the lateral mobility of membrane-bound receptors to cluster upon binding. Here we present an experimental model system that allows us to compare systematically the effects of multivalent interactions on fluid and immobile surfaces. A crucial feature of our model system is that it allows us to control the membrane surface chemistry, the properties of the multivalent binder and the binding affinity. We find that multivalent probes retain their superselective binding behaviour at fluid interfaces. Supported by numerical simulations, we demonstrate that, as a consequence of receptor clustering, superselective binding is enhanced and shifted to lower receptor densities at fluid interfaces. To translate our findings into a simple, predictive tool, we propose an analytical model that enables rapid predictions of how the superselective binding behavior is affected by the lateral receptor mobility as a function of the physico-chemical characteristics of the multivalent probe. We believe that our model, which captures the key physical mechanisms underpinning multivalent binding to biological membranes, will greatly facilitate the rational design of nanoprobes for the superselective targeting of cells.

INTRODUCTION

Multivalent binding is ubiquitous in nature, where biospecific recognition is often based on multiple ligand/receptor pair interactions.[1] As compared to monovalent binding, it provides the combination of strong adhesion (due to collective behavior) and reversibility (through disassembling multiple bonds one by one).[2] This makes biological systems sensitive to environmental changes, diagnostic and therapeutic exposures,[3,4] while offering chemists an efficient tool to develop well-organized and stimuli-responsive nanostructures.[5–7] Moreover, it has been demonstrated that multivalent probes are superselective, *i.e.*, they are able to sharply discriminate between small differences in the density of surface binders.[8,9] Furthermore, one can design multivalent probes such that they target a desired binder density,[10] which represents an attractive strategy for biomedicine because it adds a new dimension to the discrimination of different cell types.[4]

Although different determinants of multivalent binding have been identified such as the density[8–16] and the affinity[10,15,17] of surface binders, the size[11,14] and the concentration[10,11] of adhesive objects, very little is known about the role of lateral mobility and clustering. Membrane fluidity constitutes an intrinsic property of any cell surface.[18] Besides, membrane receptors that are activated *via* multivalent interactions are known to create submicrometer-sized assemblies, whose structure, composition and binding propensity markedly differ from the rest of the biointerface.[18,19] Thus activated receptors are involved in sensing and signalling, taking place in a diversity of cellular processes such as adhesion,[20] chemotaxis,[21,22] inflammation,[23] immune response[24] and secretion.[25] The lateral diffusion, the local density and the total number of activated receptors contribute to a fine-regulation of these various biological responses. Therefore, identifying the relationship between membrane fluidity, multivalent recognition and clustering is crucial for the understanding and control of biological systems.

At present the role of the lateral mobility of receptors is far from clear. On the level of a single multivalent probe, it has been proposed that a fluid surface is more efficient in mediating multivalent binding as compared to an immobile surface with the same binder density,[26] even at the cost of entropic losses resulting from the concomitant lateral translations.[27] More recent theoretical studies performed on molecular ensembles suggest that the number of surface-bound multivalent probes[28] and the induced surface clustering[29] depend supra-linearly on the density of surface binders. On the experimental side, it has been proposed that lateral mobility may affect the stability of multivalent anchoring to the surface[30] as well as its dependence on the density of surface binding sites.[16] Despite this progress there is no unified picture that would allow one to predict the behavior of a given multivalent probe (*i.e.* with a certain size, valency and concentration) at a given fluid interface (*i.e.* with a certain

binder density and affinity). Moreover, none of the reported theoretical predictions has been assessed experimentally. Either the immobilization of binder moieties limited biomimicry[8,10,12,13] or the experimental control over lateral displacements was lacking.[11,14,15,17]

Here, we present an experimental model system allowing to probe the role of lateral mobility in a quantitative and systematic way. The model is based on streptavidin/biotin recognition coupled to multivalent host/guest interactions between a linear polymer and a surface. The biopolymer hyaluronan (HA) with chemically grafted hosts is used as a model multivalent probe. The choice of HA is motivated by its ubiquitous presence in extracellular matrix of vertebrates, and its biocompatibility and use in biomedical applications.[31–33] Guests are anchored to the surface *via* specific and highly stable streptavidin/biotin recognition. This enables the same anchorage biochemistry to be applied for fluid surfaces (supported lipid bilayers, SLBs) and for immobile surfaces (self-assembled monolayers, SAMs), thus allowing one to switch lateral mobility on/off. SLBs and SAMs were chosen because of their wide use in surface engineering, well-established and tightly controlled conjugation chemistries and compatibility with various characterization techniques.[6–8,10,11,30] We use this experimental model to study how the main characteristics of multivalent binding, in particular its superselectivity, are influenced by the presence of laterally mobile binders and how this effect depends on the characteristics of the multivalent probe. Coupled to numerical simulations and analytical modelling, our study sheds light on the physical mechanisms underpinning superselective multivalent binding at fluid interfaces.

EXPERIMENTAL SECTION

Materials. HS-$(CH_2)_{11}$-EG_4-OH (EG – ethylene glycol) and HS-$(CH_2)_{11}$-EG_6-biotin were purchased from Prochimia (Sopot, Poland). Dioleoylphosphatidylcholine (DOPC) and dioleoylphospatidylethanolamine-CAP-biotin (DOPE-CAP-biotin) were purchased from Avanti Polar Lipids (Alabaster, AL). 1-Adamantaneacetic acid, O-(2-aminoethyl)-O′-[2-(biotinylamino)ethyl]octaethylene glycol (b-OEG, OEG – oligo-EG), streptavidin from *Streptomyces avidinii* (SAv, $M_w \approx 60$ kDa), atto565-labeled streptavidin (SAv-atto565), *N*,*N*-diisopropylethylamine (DIEA), hydroxybenzotriazole (HOBt) and *N*,*N*′-diisopropylcarbodiimide (DIC) were purchased from Sigma-Aldrich. Hyaluronan (HA) with a weight-averaged molecular mass M_w = 357 kDa was modified with β-cyclodextrin (β-CD) by derivatizing the HA hydroxyl groups with a degree of substitution $DS_{β\text{-}CD}$ = 21%; the synthesis has been described previously,[10] and the average molecular mass of HA-β-CD is M_w = 601 kDa. Glass coverslips (24 × 24 mm^2) were purchased from Menzel-Gläser (Braunschweig, Germany). Silicon wafers with a native oxide film were purchased from University Wafer (Boston, MA). Silicon wafers with an opaque gold coating were purchased from BT Electronics (Les Ulis, France). 4.95 MHz QCM-D sensors coated with gold (QSX301) or silica (QSX303) were purchased from Biolin Scientific (Västra Frölunda**,** Sweden). A working buffer made of 10 mM HEPES, pH 7.4 and 150 mM NaCl was used for all measurements. All experiments were performed at room temperature.

Synthesis of b-OEG-AD. A bi-functional OEG linker bearing biotin at one end and adamantane at the other (b-OEG-AD) was synthesized through an acid-amine coupling between 1-adamantaneacetic acid and b-OEG. To this end, b-OEG (50 mg, 7.32×10^{-5} mol, 1 equivalent) was dissolved in 10 mL of dry DMF followed by successive addition of DIEA (10 mg, 8.05×10^{-5} mol, 1.1 equivalents), HOBt (20 mg, 14.64×10^{-5} mol, 2 equivalents), DIC (37 mg, 29.29×10^{-5} mol, 4 equivalents) and 1-adamantaneacetic acid (28 mg, 9.52×10^{-5} mol, 2 equivalents). The resulting 15 mL mixture was stirred under N_2 for 24 h. After evaporation of ~ 80 % DMF, the residue was poured into diethyl ether. The collected precipitate was dissolved in methanol, purified *via* column chromatography (ethyl acetate:methanol = 9:1) and dried to give the final product (30 mg, 48% yield). The chemical shifts δ (in ppm) for ^{1}H NMR (D_2O, 500 MHz, 298 K) corresponding to the characteristic signal intensities are: 1.30-1.40 (*m*, 2H, 1 -CH_2- of the biotin tail), 1.45-1.75 (*m*, 4H, 2 -CH_2- of the biotin tail; 12H, 6 -CH_2- of adamantane), 1.80-2.00 (*m*, 5H, 1 -CH_2- and 3 -CH- of adamantane), 2.15-2.25 (*t*, 2H, 1 -CH_2- of the biotin tail), 2.65-2.78 (*d*, 1H, -CH_2- of the biotin head), 2.85-3.00 (*dd*, 1H, -CH_2- of the biotin head), 3.20-3.40 (*m*, 1H, -CH- of the biotin head; 4H, 2 -CH_2- of OEG), 3.49-3.72 (*m*, 36H, 18 -CH_2- of OEG), 4.28-4.43 (*m*, 1H, -CH- of the biotin head), 4.50-4.57 (*m*, 1H, -CH- of the biotin head). *m*/*z* found in TOF-MS-ES+ is 876.31, while $[M+NH_4]^+$ calculated for $C_{42}H_{74}N_4O_{12}S$ is 876.54.

Formation of b-SAMs and b-SLBs. Biotinylated self-assembled monolayers (b-SAMs) were formed on gold-coated QCM-D sensors and silicon wafers, and supported lipid bilayers (b-SLBs) were formed on silica-coated QCM-D sensors and on silicon wafers, following previously developed protocols.[30] These protocols were also adapted on glass cover slips. Coverslips were first cleaned by 1 h immersion in a freshly prepared piranha solution (H_20_2:H_2SO_4 = 1:3) followed by thorough water rinsing. To form b-SAMs, a thin gold layer (0.5 nm adhesive Ti followed by 5 nm Au) was then deposited on clean glass coverslips using a magnetron sputter system (ATC 1800 UHV; AJA International, Scituate, MA). The subsequent surface chemistry was the same as in the case of QCM-D sensors coated with gold (for b-SAMs) or silica (for b-SLBs).[30] The biotin content was fixed to 1% for b-SAMs (HS-$(CH_2)_{11}$-EG_4-OH:HS-$(CH_2)_{11}$-EG_6-biotin = 99:1) and to 0.6% for b-SLBs (DOPC:DOPE-CAP-biotin = 165:1). The quality of the formed coatings was verified by contact angle (b-SAMs) or QCM-D (b-SLBs) measurements as described previously.[30]

Fluorescence recovery after photobleaching (FRAP) measurements were performed with a confocal laser scanning microscope (LSM 700; Zeiss, Germany) using a plan-apochromat 63×/1.4 oil immersion objective and a 555 nm laser. Cleaned glass coverslips (for b-SLBs) or gold-coated glass coverslips functionalized *ex situ* with b-SAMs were used as substrates. Picodent glue (Wipperfürth, Germany) was used to attach the substrates to a custom-made Teflon holder. The surface functionalization was performed in batch mode inside the Teflon wells (volume = 50 µL). Atto565-labeled SAv served as a reporter of the lateral mobility of the SAv-bound b-OEG-AD. SAv-atto565, b-OEG-AD and HA-β-CD were incubated at 10, 20 and 50 µg/mL for 30, 20 and 60 min, respectively. The excess of each molecule was removed after each incubation step by repeated dilutions with the working buffer. After acquiring 3 pre-bleach images, a circular region (diameter = 20 µm) was bleached *via* exposure to high laser intensity for several seconds. The fluorescence recovery due to lateral diffusion of bleached and unbleached SAv-atto565 was monitored through acquisition of post-bleach images over a period of 10-15 min. The acquired images were analyzed as described previously,[34] using a custom-made time-resolved profile analysis algorithm[35] implemented in Matlab. Briefly, each image was corrected for

background fluorescence, spatial aberrations and intensity fluctuations and radially averaged. The obtained intensity profiles were compared with numerical solutions of a diffusion equation for a model with a mobile fraction and an immobile fraction. The size of the mobile fraction and its diffusion constant were fitted *via* global minimization of the root-mean-square (rms) differences between numerical predictions and experimental post-bleach profiles.

Spectroscopic ellipsometry (SE) measurements were performed on silicon wafers with a native oxide film (for b-SLBs) or with a gold coating (functionalized *ex situ* with b-SAMs) using a spectroscopic rotating compensator ellipsometer (M2000V; J. A. Woollam, Lincoln, NE) and a custom-made open cuvette (volume = 250 µL) equipped with a magnetic stirrer for liquid homogenization and connections to tubings for liquid flow. Sample incubations were performed in batch mode by injecting concentrated samples directly into the buffer-filled cuvette under stirring. SAv and HA-β-CD were incubated at 10 and 50 µg/mL, respectively. b-OEG-AD was diluted with b-OEG at desired molar ratios (between 0 and 100 %) and injected at a total concentration of 20 µg/mL. Rinsing in working buffer was performed in flow mode at a flow rate of 0.5 mL/min. The ellipsometric angles Δ and Ψ were acquired over a wavelength range from λ = 380 to 1000 nm, at an angle of incidence of 70°. The refractive index $n(\lambda)$ and optical thickness d of the adsorbed film were determined by fitting the ellipsometric data to a multilayer model using the software CompleteEASE (J. A. Woollam).[30] The adsorbed organic mass per unit area Γ was determined as:

$$\Gamma = d(n - n_{\mathrm{sol}})/(\mathrm{d}n/\mathrm{d}c) \qquad (1)$$

which is equivalent to de Feijter's equation,[36] with refractive index increments dn/dc = 0.180 cm^3/g for SAv, and 0.150 cm^3/g for HA-β-CD.[36,37] n_{sol} is the refractive index of the bulk solution, and n and n_{sol} were set to have the same wavelength dependence.

Quartz crystal microbalance with dissipation monitoring (QCM-D) measurements were performed in flow mode at a flow rate of 20 µL/min using a Q-Sense E4 system equipped with four Q-Sense Flow Modules (Biolin Scientific). Silica-coated sensors (for b-SLBs) or gold-coated sensors (functionalized *ex situ* with b-SAMs) were used as substrates. Before injection, SAv, b-OEG-AD/b-OEG and HA constructs were dissolved in working buffer to 10, 20 and 50 µg/mL, respectively. Overtones j = 3, 5, 7, 9, 11, and 13 were recorded in addition to the fundamental resonance frequency (4.95 MHz). Changes in dissipation (ΔD) and normalized frequency, $\Delta f = \Delta f_j/j$, for j = 7 are presented; all other overtones would have provided qualitatively equivalent information.

RESULTS AND DISCUSSION

Experimental analysis. Our goal was to establish how interface fluidity influences multivalent recognition. We focused on the amount of the bound multivalent probe, the stability of binding, and selectivity in the recognition of the density of surface binders (superselectivity). To this end, we developed a well-defined model interaction system that allowed quantitative tuning of the density of surface binders with surfaces designed such that binders were either laterally mobile or immobile. Particular care was taken to keep the chemistry of surface binder anchorage identical on the fluid and immobile interfaces, and to avoid any non-specific interactions of the multivalent probe with the surface.

Model design. The experimental model is based on host/guest supramolecular chemistry combined with biospecific streptavidin (SAv) / biotin (b) interactions (Fig. 1). The surface fluidity was set to OFF or ON with biotinylated self-assembled monolayers (b-SAMs; immobile, Fig. 1A) or supported lipid bilayers (b-SLBs; fluid, Fig. 1B), respectively. The surfaces were functionalized with the guest adamantane (AD). To this end, an adamantane derivative with a flexible linker and biotin (b-OEG-AD) was synthesized (**1** in Fig. 1; see experimental part for the

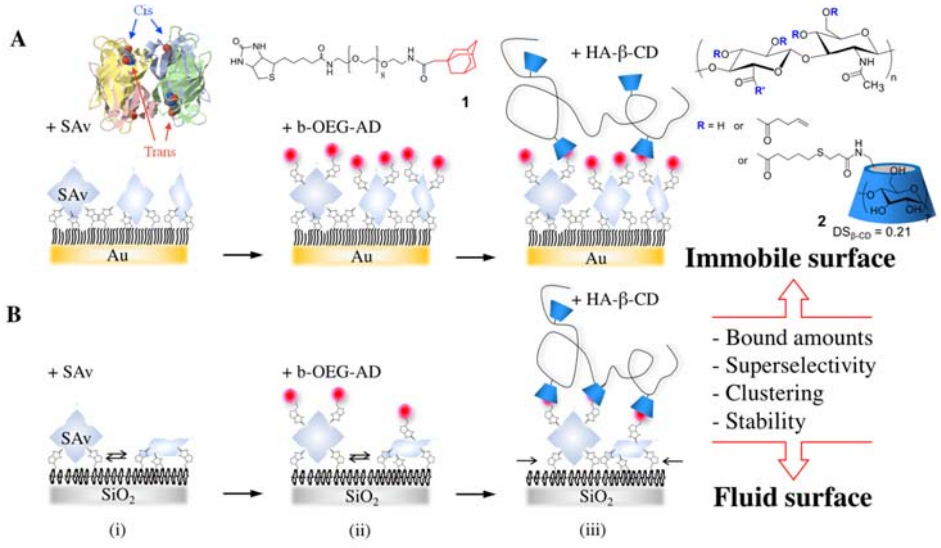

Figure 1. Experimental model system to study the role of lateral mobility in multivalent binding. A comparative study was conducted on immobile (b-SAM, A) and fluid (b-SLB, B) surfaces. The main surface functionalization steps included: (i) the immobilization of SAv on b-SAM or b-SLB, (ii) the adsorption of b-OEG-AD and (iii) the characterization of multivalent HA-β-CD binding. Lateral mobility and clustering of surface binding sites are schematically shown by arrows (B). The chemical structures of key molecules are also shown in A: SAv (ribbon diagram, each of the four monomers in distinct color) with biotins (ball-and-stick model) attached to its four binding pockets with pairwise arrangement in *cis* and *trans* when located on the same or opposite faces, respectively, of the tetramer; b-OEG-AD (biotin-(EG)$_9$-adamantane; **1**); HA-β-CD (DS = 21 %, M_w = 601 kDa; **2**). The red frame highlights the characteristics of multivalent binding whose dependence on lateral mobility was studied.

Table 1. The characteristics of the model multivalent probe: degree of substitution by β-CD ($DS_{β\text{-}CD}$), average molecular weight of HA-β-CD ($M_w^{HA\text{-}β\text{-}CD}$), average number of β-CDs per polymer chain (valency, $n_{β\text{-}CD}$), average polymer contour length between adjacent β-CDs ($l_{β\text{-}CD}$), β-CD/AD affinity (K_d), polymer radius of gyration ($R_g^{HA\text{-}β\text{-}CD}$) and polymer concentration ($c_{HA\text{-}β\text{-}CD}$).

Parameter	Value
$DS_{β\text{-}CD}$ [a]	21 %
$M_w^{HA\text{-}β\text{-}CD}$ [a]	601 kDa
$n_{β\text{-}CD}$ [b]	187
$l_{β\text{-}CD}$ [b]	5 nm
$R_g^{HA\text{-}β\text{-}CD}$ [c]	45 nm
K_d [c]	10 μM (11.5 k_BT)
$c_{HA\text{-}β\text{-}CD}$	120 nM

[a] Determined based on the weight-averaged molecular weight of HA (357 kDa) and NMR analysis of the synthesized HA-β-CD;[10] [b] calculated based on the determined $M_w^{HA\text{-}β\text{-}CD}$ and $DS_{β\text{-}CD}$; [c] taken from previous studies.[8,10]

synthesis), and linked to the biotinylated surface *via* tetravalent SAv. As multivalent probes we used HA to which the host β-CD was conjugated at a defined valency (HA-β-CD, **2** in Fig. 1; synthesis has been described elsewhere[10]). The main characteristics of HA-β-CD are summarized in Table 1.

The β-CD/guest chemistry was shown to be an excellent model for multivalent binding, mainly due to its wide affinity range (K_d = 0.01-10 mM) and well-developed conjugation chemistries.[8,10] In addition, the chemical nature of β-CD proved to be efficient in suppressing undesired non-specific polymer/polymer and polymer/surface interactions.[8] We therefore focused on a configuration where β-CD is grafted to HA while hydrophobic guests are attached to SAMs and SLBs.

The use of a SAv interlayer proved to be beneficial in that it facilitated the anchorage of AD on SAMs and SLBs using the same surface chemistry. Initially, we tested direct covalent attachment of AD via azide/alkyne click chemistry,[8,10] but this approach led to low functionality on SLBs (data not shown). We attribute this to the tendency of hydrophobic guests to embed inside the amphiphilic lipid bilayer, as indeed previously reported for different hydrophobic molecules.[38,39] The spatial separation between AD and SLB afforded by the SAv interlayer effectively prevents this undesired effect.

Special attention was paid to the molecular composition of the surface coatings. First, we used OEG as a backbone for SAMs and phosphatidylcholine as a background lipid, because these effectively suppress undesired nonspecific binding to the surfaces.[7,8,30] Second, we carefully adjusted the biotin-content of b-SAMs and b-SLBs. With 1.0 % b-SAMs, stable and close-to-maximal SAv binding was achieved and the residual density of free biotins (after SAv binding) was negligible.[30] This provided a maximal dynamic range of AD surface densities whilst avoiding undesired β-CD/biotin interactions.[40] With 0.6 % b-SLBs, approximately half-maximal SAv coverage was achieved,[30] which avoided excessive crowding thus allowing SAv diffusion along the surface. Third, we fixed the contour length of the flexible OEG linker in b-OEG-AD to 2.5 nm (9 EG units). This ensured good AD accessibility for β-CD binding, but effectively prevented immersion of AD into the hydrophobic part of the SLB. Indeed, the estimated distance from the amide bond of biotin to the b-SLB (b-SAM) surface is in the range from 2.6 to 3.2 nm, depending on SAv orientation,[30] and thus the OEG linker is too short, even in the fully stretched conformation, for AD to be able to reach the hydrophobic regions within the SLB or SAM. A similar surface chemistry was successfully applied to lipid vesicles, which additionally supports the efficiency of β-CD/AD interactions in our model.[41]

Model characterization. We ascertained successful preparation of the model surfaces with a set of surface analysis techniques. Spectroscopic ellipsometry (SE) was used to quantify the surface density of macromolecules, fluorescence recovery after photobleaching (FRAP) to probe their lateral mobility, and quartz crystal microbalance (QCM-D) to verify binding specificity.

The average AD surface density (Γ_{AD}) could not be measured directly by SE because of the low molecular weight of b-OEG-AD. Instead, it was quantified as:

$$\Gamma_{AD} = \Gamma_{SAv} \times b \times x \quad (2)$$

where Γ_{SAv} is the SAv surface density; b is the SAv residual valency, *i.e.* the average number of biotin-binding sites that remain per SAv after its attachment to the surface; x is the molar b-OEG-AD/b-OEG ratio on the surface, where b-OEG (the precursor for the synthesis of b-OEG-AD) is used as a diluting agent to tune the AD surface density. Assuming the binding of the molecules being mass transport limited, x was determined as $x = (r_{b-OEG}/r_{b-OEG-AD})^{2/3} \times x'$, where r is the hydrodynamic radius of the molecule and x' is the molar b-OEG-AD/b-OEG ratio in solution. With estimated r = 0.52 nm for b-OEG and 0.58 nm for b-OEG-AD,[42] we find $x = 0.93\,x'$ implying that the mixing ratio on the surface is close to that in the solution. Γ_{SAv} was measured by SE, and b was also determined by SE using a biotinylated reporter probe (Supporting Fig. S1). This analysis showed that SAv binds to two biotins on 1 % b-SAMs (b = 1.96 ± 0.03) and to between two and three biotins on 0.6% b-SLBs (b = 1.50 ± 0.05). This is in good agreement with previous work where we had analyzed the residual valency more systematically for b-SAMs and b-SLBs and demonstrated that SAv can bind in several distinct orientations on these surfaces: divalent in *cis* or *trans* (where this refers to the arrangement of biotin-binding sites in SAv) and trivalent.[30] The maximal AD surface densities (x = 1) were found to be 6.6 pmol/cm^2 on b-SAMs and 2.6 pmol/cm^2 on b-SLBs. We note that in our model, the minimal AD-AD spacing (l_{AD}) is limited to the distance between the adjacent biotin-binding sites of SAv, which

Table 2. The characteristics of the model surfaces: biotin-biotin root-mean-square (rms) distance (l_b), surface density of SAv (Γ_{SAv}), SAv-SAv rms distance (l_{SAv}), residual valency of the adsorbed SAv (b), maximal surface density of guests (Γ_{AD}^{max}), size and the diffusion constant of the mobile fraction. The determined experimentally values are presented as mean ± standard error.

Parameter	**1.0% b-SAM**	**0.6% b-SLB**
l_b, nm [a]	5.3	10.0
Γ_{SAv}, pmol/cm^2 [b]	3.36 ± 0.15	1.75 ± 0.09
l_{SAv}, nm [c]	7.0 ± 0.2	9.7 ± 0.3
b [d]	1.96 ± 0.03	1.50 ± 0.05
Γ_{AD}^{max}, pmol/cm^2 [e]	6.6 ± 0.4	2.6 ± 0.2
Mobile fraction, % [f]	< 1	84 ± 1
Diffusion constant, μm^2/s [f]	-	0.86 ± 0.01

[a] Calculated assuming the molar fraction of biotinylated thiols/lipids present on the surface is identical to the molar fraction in the solution from which b-SAMs/b-SLBs are assembled; [b] determined by SE ($n \geq 7$); [c] calculated from Γ_{SAv}; [d] determined by SE (n = 2) using biotinylated reporter probes as described previously, with corresponding data shown in Fig. S1;[30] [e] calculated as $\Gamma_{AD}^{max} = \Gamma_{SAv} \times b$ (x = 1); [f] determined by FRAP through time-resolved profile analysis (see experimental section).

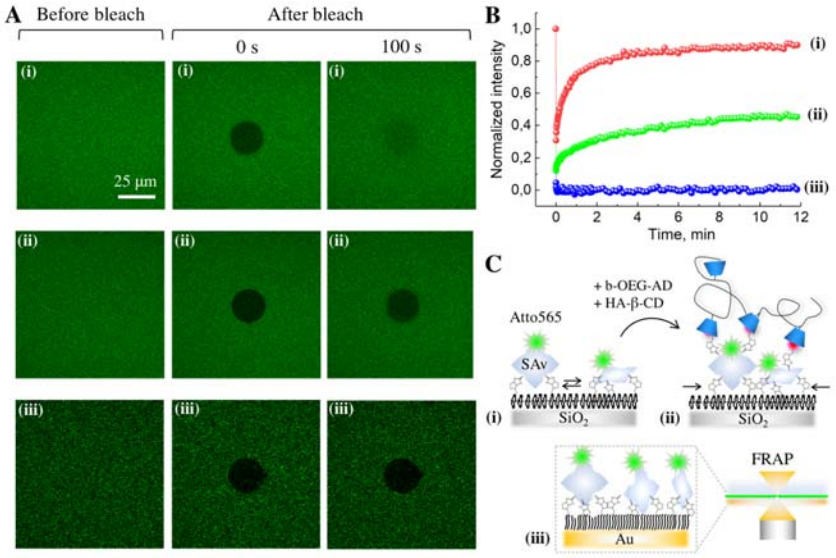

Figure 2. FRAP characterization of surface fluidity. SAv-atto565 serves as a reporter of the lateral mobility of the surface-bound b-OEG-AD. Measurements are performed at the interface of the solid substrates coated with the organic films and the working buffer (see experimental section for sample preparation). Bleaching is done by exposure of a circular region to high laser intensity for several seconds. (A) Representative micrographs taken before and after photobleaching of b-SLBs (i) and b-SAMs (iii). In the case of b-SLBs, the measurement was repeated after the successive adsorption of b-OEG-AD (x = 1) and HA-β-CD (ii). (B) Kinetics of the fluorescence recovery through lateral diffusion of SAv-atto565. The fluorescence intensity of the bleached spot, normalized against the fluorescence intensity of the non-bleached region of the same size (to correct for bleaching during image acquisition and drift effects) and background corrected for unbleached fluorescence (estimated from (iii)), is plotted *versus* time. (C) Schematics of the three studied systems together with the FRAP setup.

corresponds to 2.0 and 3.5 nm for SAv bound to biotinylated surfaces in divalent *cis* and divalent *trans* orientations.[30] We also point out that the dilution of b-OEG-AD ($0 < x < 1$) results in a reduced effective valency, meaning that a mix of SAv complexes with 0, 1 or 2 ADs are present on both immobile and fluid surfaces. Table 2 summarizes the main characteristics of the model surfaces.

A fluorescent SAv was used with otherwise unaltered surface preparation to test the fluidity of the model surfaces by FRAP (Fig. 2). Close-to-complete fluorescence recovery was observed on b-SLBs (Fig. 2, sample i) whereas there was no recovery on b-SAMs (Fig. 2, sample iii), confirming the two distinct fluid and immobile states of these two interfaces. Quantitative analysis yielded a mobile fraction of 84 ± 1 % and a diffusion constant of 0.86 ± 0.01 µm^2/s for SAv on the SLBs (Table 2), and FRAP characteristics were found essentially unaltered when AD was bound to SAv (Supporting Fig. S2). This validates the use of SAv-atto565 as a reporter probe for the lateral mobility of AD. Remarkably, a drastic decrease of FRAP kinetics was detected after the addition of HA-β-CD (Fig. 2, sample ii), indicating a strong multivalent binding between the polymer and the fluid surface. A decrease in the mobile fraction to 40 ± 1 % and a reduction in the diffusion constant to 0.15 ± 0.01 µm^2/s suggest that approximately half of the SAv (with bound ADs) slow down while the other half is effectively immobile after HA-β-CD binding over the timescale probed. These two fractions can be attributed to ADs bound to SAv with residual valencies 1 and 2 which are present approximately at 1:1 ratio on 0.6% b-SLBs (Table 2), suggesting that long range motion (over the µm range probed by FRAP) is effectively inhibited for divalent but not monovalent surface binders by attachment of polyvalent HA-β-CD.

Additional control measurements by QCM-D (Supporting Fig. S3) showed that b-OEG-AD does not bind to b-SLBs/b-SAMs lacking SAv, or to SAv monolayers lacking free binding sites for biotin. These results demonstrate that b-OEG-AD binds to our model surfaces through specific biotin/SAv interactions, which provides us with quantitative control on the AD surface density.

The specificity of multivalent recognition was also characterized. To this end, we monitored by QCM-D the binding of SAv, b-OEG-AD and several HA constructs (HA, HA$_p$ and HA-β-CD) to b-SAMs and b-SLBs (Supporting Fig. S4). HA and HA$_p$ are the precursors for the synthesis of HA-β-CD, non-modified and modified with pentenoate, respectively.[10] The obtained QCM-D data revealed strong interaction between HA-β-CD and SAMs/SLBs displaying AD, whereas binding between HA lacking β-CD and SAMs/SLBs displaying AD, and between HA-β-CD and SAMs/SLBs lacking AD, was virtually absent except for a minor amount (just above the detection limit) of reversible binding. By SE we measured residual responses at x = 0 of approximately 1.7 fmol/cm^2 HA-β-CD on SLBs and 3.3 fmol/cm^2 on SAMs that were reversible upon rinsing with buffer; these might in part be due to minimal changes in the refractive index of the bulk solution during HA-β-CD incubation affecting the data analysis. In contrast, up to 60 fmol/cm^2 were observed with AD (*vide infra*). These results demonstrate that HA-β-CD binding to our model surfaces has a very low contribution of non-specific binding and thus is mediated essentially by specific β-CD/AD interactions.

Effect of lateral mobility on binding efficiency and superselectivity. Having established the quality of the model systems we quantified by SE how the amount of the bound multivalent probe and the stability of its anchoring to the surface depend on the surface fluidity and the density of the surface binders. Each SE experiment comprised: SAv attachment to the biotinylated surface, SAv conjugation with b-OEG-AD and HA-β-CD binding for 2 h; each step being followed by thorough buffer rinsing. Two parameters were varied independently: AD lateral mobility was either OFF (b-SAMs) or ON (b-SLBs), and the AD surface density was tuned (by diluting b-OEG-AD with b-OEG, $0 < x < 1$). Example binding data are shown in Fig. 3A

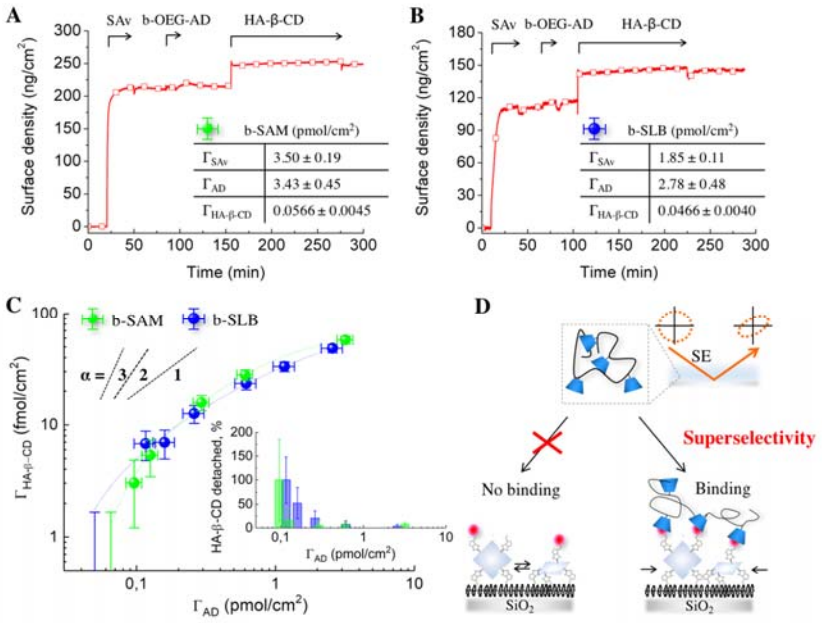

Figure 3. Effect of surface fluidity on superselective binding – experimental data. Examples of binding curves obtained by SE for SAv, b-OEG-AD and HA-β-CD on a b-SAM (A, $x = 0.5$) and a b-SLB (B, $x = 1$). Surface densities, Γ_{SAv}, Γ_{AD} and $\Gamma_{HA\text{-}\beta\text{-}CD}$, are shown in inset tables as mean ± error, where the latter is the sum of the detection limit of the SE setup (1 ng/cm^2) and a reproducibility error of 5% that was estimated from 8 (for b-SLB) and 7 (for b-SAM) measurements of Γ_{SAv} (see Table 2). (C) Experimental characterization of HA-β-CD selectivity to Γ_{AD}-presenting surfaces (log-log scale). Curves presented in (A) and (B) correspond to the two rightmost data points. For the lowest $\Gamma_{HA\text{-}\beta\text{-}CD}$, only an upper limit is given, corresponding to the sensitivity of the SE setup. Dashed lines are guides for the eyes. Slopes corresponding to $\alpha = 1$, 2, and 3 are shown to facilitate data interpretation. The inset shows the percentage of specifically bound HA-β-CD that subsequently detaches from the surface during buffer rinsing. The characteristics of HA-β-CD and model surfaces are listed in Tables 1 and 2, respectively. (D) Schematic representation of superselective binding of HA-β-CD to a laterally mobile b-SLB functionalized with SAv and b-OEG-AD, together with the SE setup.

for a b-SAM ($x = 0.5$) and in Fig. 3B for a b-SLB ($x = 1$). From such measurements, we quantified the amount of HA-β-CD ($\Gamma_{HA\text{-}\beta\text{-}CD}$) that is specifically bound at equilibrium (*i.e.*, prior to rinsing and subtracting the minor residual responses measured at $x = 0$).[†] The obtained $\Gamma_{HA\text{-}\beta\text{-}CD}$ values are shown in Fig. 3C as a function of AD surface density, and represent the most important experimental data of this study.

Clearly, the surface fluidity does not affect the overall dependence of $\Gamma_{HA\text{-}\beta\text{-}CD}$ on Γ_{AD}. On both b-SAMs and b-SLBs, the strongest dependence was observed for Γ_{AD} between 0.05 and 0.2 pmol/cm^2, whilst HA-β-CD binding was below the detection limit at lower guest surface densities and the dependence of $\Gamma_{HA\text{-}\beta\text{-}CD}$ on Γ_{AD} progressively decreased towards higher Γ_{AD}.

In order to quantify the selectivity for the surface binder density, the parameter α has been introduced[9] which measures the rate of the relative change of the number of bound objects with the relative increase in the density of surface binders, *i.e.* in our case:

$$\alpha = \frac{\mathrm{d}\,\Gamma_{HA-\beta-CD}/\Gamma_{HA-\beta-CD}}{\mathrm{d}\,\Gamma_{AD}/\,\Gamma_{AD}} = \mathrm{d}\ln\Gamma_{HA-\beta-CD}/\mathrm{d}\ln\Gamma_{AD} \qquad (3)$$

When α exceeds 1, HA-β-CD binding increases faster-than-linearly with AD density:

$$\Gamma_{HA-\beta-CD} \propto \Gamma_{AD}^{\alpha} \qquad (4)$$

and this defines the regime of superselective binding. The steepest slopes in the log-log plot shown in Fig. 3C are larger than α = 2, implying that the binding of HA-β-CD is indeed superselective. Whilst this is in agreement with our previous work on immobile surfaces,[8,10] our current experiments demonstrate that such superselective binding is essentially unaffected by surface fluidity. This is the most important result of our study.

We also examined the stability of binding, which is expressed as the fraction of HA-β-CD released upon rinsing, *i.e.*, $\Gamma^{det}_{HA-\beta-CD}/\left(\Gamma_{HA-\beta-CD} + \Gamma^{det}_{HA-\beta-CD}\right)$, where $\Gamma^{det}_{HA-\beta-CD}$ is the amount of detached HA-β-CD (as for $\Gamma_{HA-\beta-CD}$, $\Gamma^{det}_{HA-\beta-CD}$ was corrected for non-specific binding). The obtained data shows that the stability of HA-β-CD anchoring is also largely independent of surface fluidity (Fig. 3C, inset). At high Γ_{AD}, binding was essentially irreversible with less than 10 % of detachment, while the reversibility became pronounced at $\Gamma_{AD} < 0.3$ pmol/cm^2. We speculate that the reversible fraction comprises mostly monovalent interactions with possible small contribution from unfavorable multivalent bonds, *i.e.*, when conformational entropic costs due to steric restrictions (at high coverage) or insufficient AD density (at low coverage) are not balanced by the enthalpic gains through the complexation of one or a few β-CD/AD pairs.

Numerical simulations. The experimental data provided direct evidence that the superselective nature of HA-β-CD binding is essentially unaffected by surface fluidity, but could not reveal how HA-β-CD binding affects the distribution of AD on the surface and what the typical valency of interaction is. To address these questions, we resorted to numerical computer simulations.

Grand canonical Monte Carlo simulations were performed using the soft blob model that we have described in previous work.[10] This model explicitly considers the polymeric nature, valency and size of HA-β-CD, and was here extended to fluid surfaces (see Supporting Methods for details). From Fig. 4A,

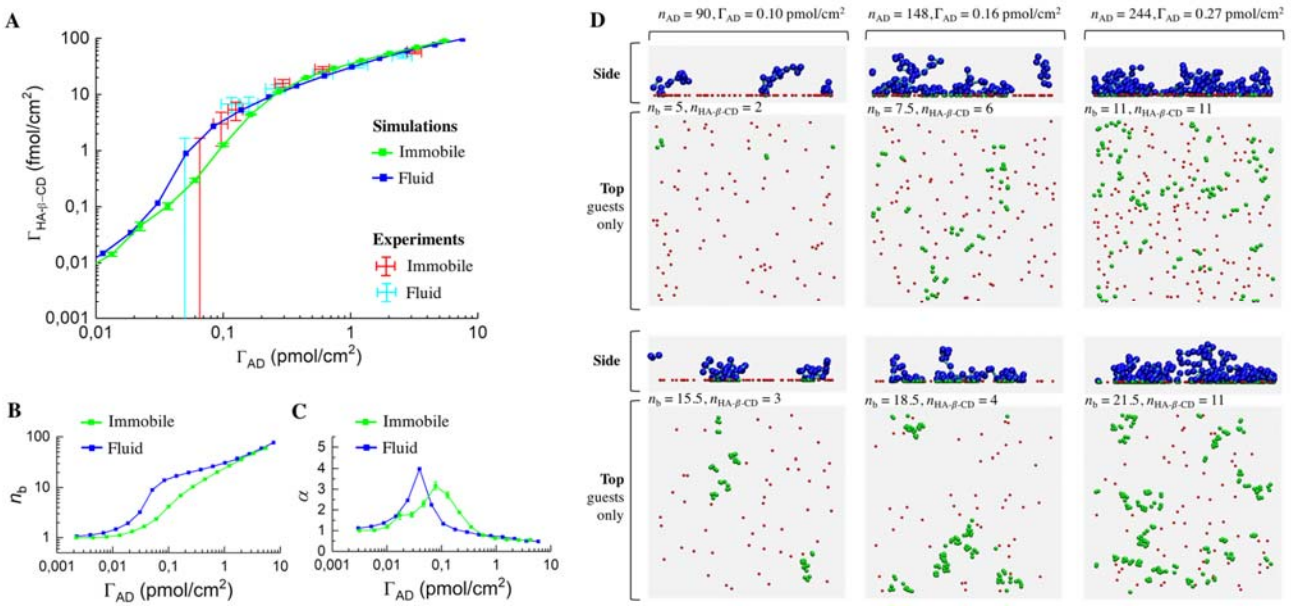

Figure 4. Effect of surface fluidity on superselective binding - numerical simulations. (A) HA-β-CD binding *vs* AD surface density (log-log scale) for immobile (green) and fluid (blue) surfaces. Lines with symbols are predictions from simulations. Each data point represents a single simulation run (fluid) or mean ± SE calculated from 100 independent runs (immobile) with solid lines connecting data points; higher statistics allowed to reduce the effect of random guest positions on polymer adsorption at low Γ_{AD} and thus improve the reproducibility in the immobile case. For comparison, experimental data are also shown for immobile (red) and fluid (cyan) surfaces as error bars (taken from Fig. 3C). (B) Average valency of binding n_b determined through numerical simulations is plotted *vs* Γ_{AD}. (C) α extracted from the simulation data is plotted *vs* Γ_{AD}. Conditions: polymer characteristics were fixed to that of HA-β-CD (Table 1); the number of blobs per polymer (m_b) and the host/guest binding energy (F) were fixed to 20 and -3 k_BT, respectively, determined from previous work on HA-β-CD binding;[10] the lateral size of the simulation box was $L_x = L_y \approx 5R_g^{HA\text{-}\beta\text{-}CD}$. (D) Representative side- and top-view snapshots from the simulations for polymer binding to immobile (top row) and fluid (bottom row) surfaces. In the side views, chains of blue blobs and cyan joints represent polymers with hosts (β-CD), while red and green spheres correspond to non-bound and bound guests (ADs), respectively. In the top views, only the guests are shown. The number of guests in the simulation box (n_{AD}) and their corresponding molar surface density (Γ_{AD}), the number of bound polymers in the simulation box ($n_{HA\text{-}\beta\text{-}CD}$) and the average number of bonds per polymer (n_b) are indicated in each case.

one can see that the simulations allowed us to assess the effect of surface fluidity over a wider range of Γ_{AD} as compared to experiments. From the simulation data, we also extracted the average valency of interaction n_b (the average number of bonds formed per polymer) and the selectivity parameter α (Eq. 3) as a function of Γ_{AD} (Fig. 4B-C).

Relation between lateral mobility, multivalent recognition and clustering. Given that the simulated curves were obtained independently (*i.e.* not by fitting the present experimental data), they show rather good agreement with the experiments. In particular, the magnitude of binding is reproduced well, and it is also notable that the slight reduction in binding on fluid surfaces at high guest surface densities ($\Gamma_{AD} > 0.2$ pmol/cm^2) and a transition to the opposite trend at moderate guest densities ($0.05 < \Gamma_{AD} < 0.2$ pmol/cm^2), although barely noticeable in the experiments, are reproduced well by the simulations (Fig. 4A). Furthermore, simulations allowed exploration of binding at very low guest surface densities ($\Gamma_{AD} < 0.1$ pmol/cm^2) where the experiments were limited by the detection limit of SE. Remarkably, this revealed a pronounced difference between the immobile and fluid cases. For Γ_{AD} between 0.04 and 0.1 pmol/cm^2, binding was substantially (up to several fold) larger on fluid surfaces (Fig. 4A). It is particularly interesting that the observed difference is in the opposite sense as compared to high coverages, with a crossing between the two curves being located at $\Gamma_{AD} = 0.25$ pmol/cm^2. The fact that the two curves cross over suggests several binding regimes, in which lateral mobility plays different roles. Based on the simulation data, we have identified four distinct binding regimes (Fig. 4): at lowest and highest guest surface densities ($\Gamma_{AD} < 0.02$ pmol/cm^2 and $\Gamma_{AD} > 3$ pmol/cm^2, respectively, in our model), surface fluidity does not affect binding; at moderate densities (0.02 pmol/cm$^2 < \Gamma_{AD} < 0.2$ pmol/cm^2), surface fluidity enhances binding; at high densities (0.2 pmol/cm$^2 < \Gamma_{AD} < 3$ pmol/cm^2), surface fluidity reduces binding.

In order to rationalize the existence of several binding regimes, we analyzed n_b *vs* Γ_{AD} dependencies derived from the simulation data (Fig. 4B). One can see that at the lowest and highest guest densities, the immobile and fluid cases behave similarly, with binding being essentially monovalent at low guest densities and valencies reaching values of several 10s at high guest densities. Between these extremes, there is a broad region where the binding is essentially multivalent and the number of formed bonds per polymer is significantly higher for the mobile guests. An increase of up to several fold in n_b compared to immobile guests suggests that multivalent binding induces clustering on fluid surfaces. In order to visualize the effect of lateral mobility on the 2D distribution of surface binders, we extracted a series of simulation snapshots at moderate and high surface coverages (Fig. 4D). The obtained images show that the recruitment of mobile guests is indeed accompanied by their clustering, the latter being clearly visible in the top views.

Based on the obtained information about n_b (Fig. 4B) and clustering (Fig. 4D), we conclude that both promoting and inhibiting effects of lateral mobility are related to higher n_b on fluid surfaces, resulting from the ability of multivalent polymers to recruit additional mobile guests. At moderate surface coverages, this leads to the local enrichment of surface guests

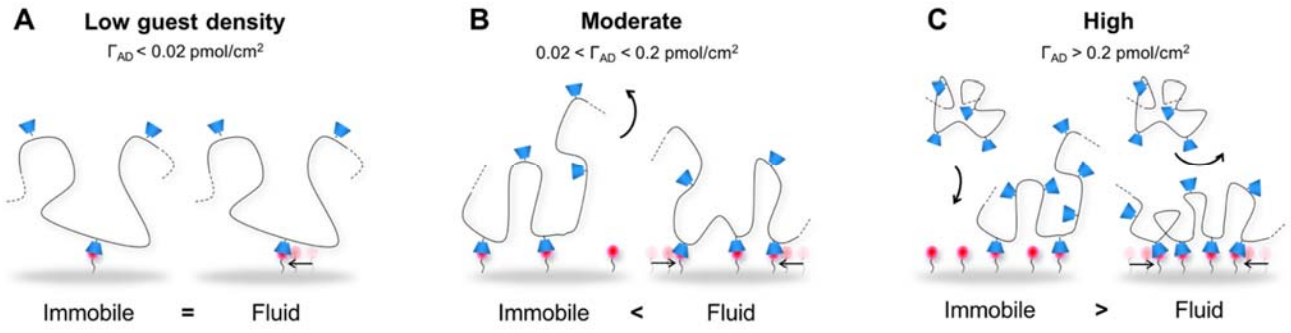

Figure 5. Distinct binding regimes occurring at different guest surface densities. Schematics show binding of host-modified polymers to immobile and fluid surfaces displaying low (A), moderate (B) and high (C) guest surface densities. At low guest coverage (in our model system, Γ_{AD} < 0.02 pmol/cm^2), binding is monovalent and the number of bound polymers is the same for immobile and fluid cases (linear regime). At moderate guest coverage (0.02 < Γ_{AD} < 0.2 pmol/cm^2), binding becomes multivalent and recruitment of additional guests occurs in the fluid case, which increases overall binding (local enrichment of guests). At high guest coverage (Γ_{AD} > 0.2 pmol/cm^2), the initially adsorbed polymers recruit most of the laterally mobile guests, which limits further multivalent interactions and thus decreases overall binding (global depletion of guests). A fourth regime of very high guest surface densities is not shown here, where steric exclusion limits polymer binding and the number of bound polymers is again the same for immobile and fluid cases.

(see snapshots at Γ_{AD} = 0.1 pmol/cm^2, Fig. 4D), thus promoting multivalent binding of individual polymers. This explanation is in agreement with previous theoretical studies, which assessed the role of lateral mobility at a single polymer level.[26] At high surface coverages, along with the local enrichment a global depletion of guests occurs (see snapshots at Γ_{AD} > 0.2 pmol/cm^2, Fig. 4D). The resulting lack of free guests inhibits subsequent multivalent interactions, thus limiting the binding of additional polymers on fluid surfaces as compared to the immobile ones. The main features of the identified binding regimes, consistently found in experiment and simulations, are summarized in Fig. 5.

Influence of lateral mobility on superselectivity. The extended range of $\Gamma_{HA\text{-}\beta\text{-}CD}$ *vs* Γ_{AD} dependences (Fig. 4A) allowed us to study in more detail the relationship between lateral mobility and superselectivity. The evolution of α with Γ_{AD} extracted from the simulation (Fig. 4C) shows that the identified binding regimes (Fig. 5) differ significantly in terms of the HA-β-CD selectivity to the density of surface guests. At low Γ_{AD}, polymer coverage increases linearly with Γ_{AD} (α ≈ 1), which is expected for monovalent interactions (n_b ≈ 1, Figs. 4B and 5A). At moderate Γ_{AD} (Fig. 5B), multivalent binding dominates, exhibiting superselective behavior (α > 1). Finally, at high Γ_{AD} (Fig. 5C), the HA-β-CD uptake decreases progressively (to α < 1) as binding saturates. Whilst our experimental data already demonstrated superselective binding on fluid and on immobile surfaces (Fig. 3C), the detailed analysis afforded with the numerical simulations revealed two subtle effects of surface fluidity: (i) the quality of superselectivity is improved, and (ii) the region of optimal superselectivity shifts to lower guest densities. In our model, these effects are reflected in the increase of α_{max} from 3.2 to 4.0 and in the shift of $\Gamma_{AD}^{\alpha_{max}}$ from 0.08 to 0.04 pmol/cm^2 for fluid *vs* immobile surfaces (Fig. 4C). Both effects can be understood when looking at the n_b dependence on Γ_{AD} (Fig. 4B). In the fluid case, the multivalency onset (n_b > 1) appears earlier causing the translation of the α > 1 region to lower Γ_{AD}, followed by a steeper growth of n_b which gives rise to higher α_{max}.

High vs low guest occupancy regimes. The simulation snapshots in Fig. 4D illustrate that a substantial fraction of surface binders located within the radius of gyration of HA-β-CD can engage in bonds at a given time. We define this condition as 'high guest occupancy' regime. The regime of 'low guest occupancy' would accordingly imply that n_b remains much lower than the average amount of surface binders per $\boldsymbol{\pi R_g^2}$. In this regime, the lateral mobility of guests does not significantly affect the polymer adsorption. This is demonstrated in Supporting Fig. S5, as well as, the theoretical analysis presented below.

In summary, the simulations (Figs. 4 and S5) provided a good idea of how surface fluidity and the associated clustering of surface binders affect multivalent (and superselective) binding. In particular, they demonstrated that surface fluidity affects the range and quality of superselectivity in the regime of high guest occupancy, which is accompanied by pronounced clustering around $\Gamma_{AD}^{\alpha_{max}}$, and that these effects are reduced at low occupancy of guests. They are computationally costly, however, making it difficult to explore a large parameter space. To study in more detail the relation between the nature of the multivalent probe, the occupancy of surface binders and the role of lateral mobility, we modelled our system analytically.

Analytical modeling. The main goal of the analytical modeling was to study how the relationship between surface fluidity and multivalent binding depends on the physico-chemical parameters of the multivalent probe. Besides, we aimed to test if a simple analytical theory can predict the binding of multivalent probes at fluid interfaces quantitatively as this would be useful for the rational design of probes able to superselectively target a desired density of surface binders.

Theoretical analysis was based on the coarse-grained model developed for the adsorption of multivalent polymers to surfaces.[10,43] A detailed description of the model is provided in the Supporting Methods, and a Supporting Matlab script is also provided to calculate binding profiles. Briefly, the model assumes the surface to be covered by an array of lattice sites of size a, each containing n_g guests ($n_g = \Gamma_{AD} N_A a^2$) and surrounded by the volume $a^3 = (4\pi/3)R_g^3$ (Fig. 6A inset). In the immobile case, the number of adsorbed polymers per lattice site is calculated using a generalized Langmuir treatment, followed by Poisson averaging (Eq. S8). In the fluid case, the number of guests is allowed to equilibrate between different lattice sites.[28] In both cases, the model explicitly considers the gains in combinatorial entropy with increasing guest surface density and/or polymer valency.

Fig. 6A shows $\Gamma_{HA\text{-}\beta\text{-}CD}$ *vs* Γ_{AD} and α *vs* Γ_{AD} plots obtained for the conditions matching our experiments. Note that no

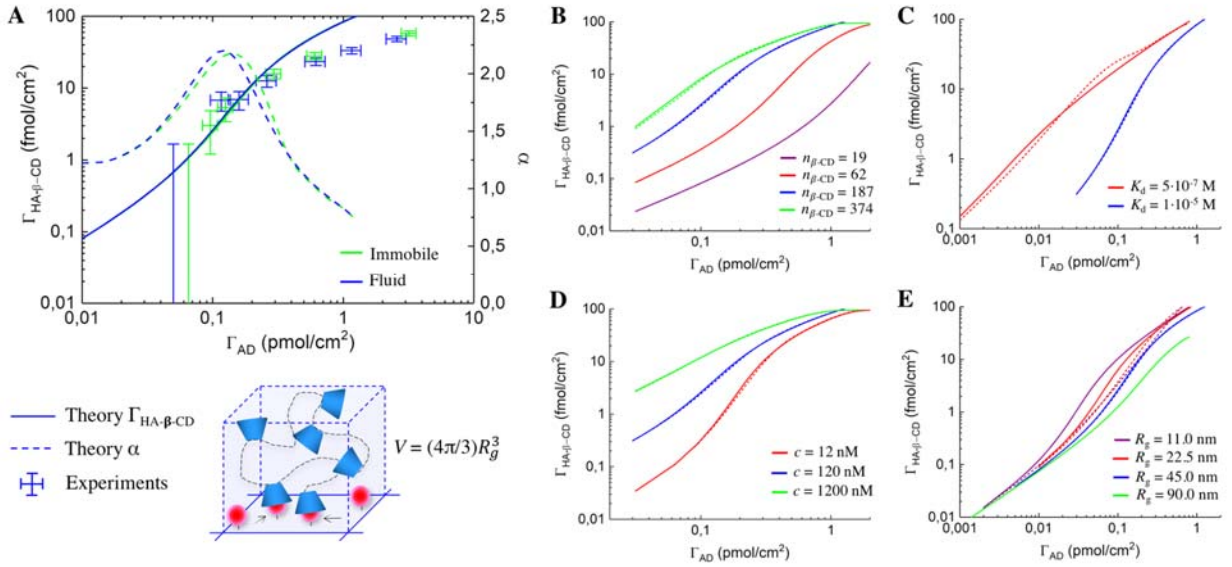

Fig. 6. Analytical modeling at tunable polymer characteristics. (A) Left ordinate axis: superposition of the analytical predictions (solid lines) for the immobile (green) and fluid (blue) surfaces with experimental binding isotherms (error bars). Right ordinate axis: superselectivity parameter, α, extracted from the theoretical data and plotted *vs* Γ_{AD} (dashed lines). The lattice site of size *a* containing n_g mobile guests and their recruitment by $n_{\beta\text{-}CD}$ hosts present in the volume of a^3 are illustrated below the plot. Polymer properties are listed in Table 1; see Supplementary Methods for details of the model parameters. (B-E) Analytical predictions for the fluid (solid) and immobile (dashed) cases obtained at tunable $n_{\beta\text{-}CD}$ (B), K_d (C), *c* (D) and R_g (E). The graphs show $\Gamma_{HA\text{-}\beta\text{-}CD}$ plotted *versus* Γ_{AD}. The corresponding dependences of α *versus* Γ_{AD} are shown in Fig. S6. Blue curves in all graphs correspond to the reference system (Table 1).

parameters were fitted, all model parameters were taken from our previous work.[10] The theoretical model overshoots at high $\Gamma_{HA\text{-}\beta\text{-}CD}$, due to underestimation of polymer excluded volume effects.[10] The model reproduces all simulation trends with regard to the effect of lateral mobility on multivalent binding. Indeed, it predicts crossing between the immobile and fluid $\Gamma_{HA\text{-}\beta\text{-}CD}$ *vs* Γ_{AD} curves at Γ_{AD} = 0.27 pmol/cm² which is very close to the value obtained from simulations (0.25 pmol/cm²; Fig. 4A) thus highlighting the existence of several distinct binding regimes (Fig. 5). In addition, the model reproduces correctly the shift of α_{max} to lower Γ_{AD}, accompanied by higher α_{max} values for fluid surfaces. This demonstrates that the analytical model, despite its simplifying treatment of the polymer and a lower magnitude of observed effects compared to numerical simulations, still allows one to assess the role of lateral mobility in the regime of high guest occupancy ($n_b \approx n_g$) as well as to quantitatively predict (Eq. 4) the position of the superselectivity range.

Furthermore, in the Supporting Methods we analytically show that the crossing point between fluid and immobile binding curves always exists. Additionally, the fluid and immobile cases must converge both at low and high guest density limits. These theoretical results directly support the distinct binding regimes illustrated in Fig. 5.

For completeness, we show in Fig. 6B-E analytical predictions over a larger parameter range, *i.e.*, at tunable polymer valency, affinity, concentration and size. The comparison of binding isotherms obtained for fluid (solid lines) and immobile (dashed lines) surfaces shows that the effect of lateral mobility on multivalent binding increases with polymer valency (Fig. 6B) and affinity (Fig. 6C), but decreases with polymer concentration (Fig. 6D) and size (Fig. 6E). As suggested by numerical simulations, the effect of lateral mobility is due to the ability of multivalent polymers to alter the 2D distribution of guests, which is reflected in higher n_b and concomitant guest clustering (Fig. 4). One would indeed expect this ability to improve when diluting polymers at high valency and/or affinity, reducing their size (i.e. increasing host density at given valency) or exposing them to low guest densities. We note that the identified trends are peculiar to the regime of high guest occupancy ($n_b \approx n_g$). In the case of low guest occupancy ($n_b \ll n_g$), the difference between the immobile and fluid cases vanishes, which follows from the model formalism (Eq. S14) and is illustrated by simulations and theoretical predictions obtained for low polymer valencies (Figs. S5 and 6B). In this regime, the scaling relation

$$x_S \propto \Gamma_{AD} n_{\beta-CD} K_d^{-1} \quad (5)$$

derived in previous work for immobile surfaces[10] can be directly applied to fluid surfaces as well, to predict in a simple way how the valency of the multivalent probe ($n_{\beta\text{-}CD}$) and the affinity of the individual interactions (K_d) shift the binding isotherm ($\Gamma_{HA\text{-}\beta\text{-}CD}$ *vs* Γ_{AD}) along the *x* axis. We also provide a Supporting Excel spreadsheet to calculate binding profiles in the low guest occupancy regime.

SUMMARY AND CONCLUSIONS

In this work, we have combined experiments, simulations and analytical modeling to understand how the fluidity of the binding interface affects multivalent binding and superselectivity. The developed model provided the first quantitative experimental demonstration of superselective multivalent recognition at fluid surfaces. Furthermore, combining experiments with simulations allowed us to assess the role of lateral mobility in a wide parameter range and to rationalize its effect on the bound amounts and superselectivity in terms of the number of formed bonds and their clustering (Figs. 4 and 5). In addition, the developed analytical model proved to be efficient for a systematic study of multi-parameter systems like the ones involving the effects of multivalency, superselectivity and lateral mobility (Fig. 6). Due to its versatility towards the nature of multivalent probe, one can use it to rationalize superselective behavior of different multivalent scaffolds (polymers, particles, etc.).[8,9,43] We note that our model does not consider any intrinsic clustering of surface binders that may occur at biointerfaces[18] in addition to the

here-reported clustering induced by multivalent probes; an interesting future avenue is to explore how intrinsic clustering is enhanced by multivalent probes. The here-obtained insights are summarized below.

i) When surface binders are in large excess (low binder occupancy), the effect of lateral mobility is negligible. The dependence of superselectivity on affinity and valency of the multivalent probe can be rationalized *via* the scaling parameter x_S (Eq. 5). Application of the generalized model is required to predict the effects of the multivalent probe's size and concentration (Eq. S14).

ii) When the number of bonds is comparable to the total number of surface binders (high binder occupancy), the effect of lateral mobility is appreciable. The influence of affinity, valency, size and concentration of the multivalent probe on superselective behavior can be predicted using the full models for immobile (Eq. S8) and fluid (Eq. S13) surfaces. The following phenomena contribute to the impact of surface fluidity on multivalent binding.

ii.i) Lateral mobility increases the number of formed bonds between the surface and the multivalent probe, which is accompanied by the clustering of surface binders.

ii.ii) The effect of lateral mobility on the amount of bound multivalent probe depends on the density of surface binders: binding is enhanced at moderate densities due to local accumulation of binders and reduced at high densities due to global depletion of binders. There is no effect at very low and very high binder densities.

ii.iii) Lateral mobility shifts the regime of superselective binding towards lower densities of surface binders and slightly improves the quality of superselectivity. These effects arise from the clustering of surface binders and the associated enhancement in combinatorial entropy.[9,28]

Scenarios involving mobile surface binders are of great relevance for the understanding and control of biological systems. In most instances, the average density of receptors on the cell surface is relatively low. For the main HA-receptor CD44, for example, which is among the most abundant receptors on various cell types, average distances of many 10s of nm have been estimated.[11,44] Considering that HA (in the extracellular matrix) and multivalent probes (for biomedical applications) have sizes in the range of 10s to 100s of nm, this implies that the 'moderate surface density' regime (Fig. 5B) is likely to occur frequently on the cell surface. It can hence be expected that mobility and clustering affect cell surface binding substantially in many biological systems. The obtained knowledge, thus, should facilitate rationalizing multivalent binding to biological membranes, and thereby contribute to understanding the mechanisms of cellular communication and, through application for the design of multivalent probes, to the continuous progress of nanomedicine.

ASSOCIATED CONTENT

Supporting Methods, Figures S1−S6, Analytical Equations and References, a Matlab script and an Excel spreadsheet to calculate binding profiles are available free of charge via the Internet at http://pubs.acs.org.

AUTHOR INFORMATION

Corresponding Authors

*galina.dubacheva@ens-paris-saclay.fr
*r.richter@leeds.ac.uk

Author Contributions

‡These authors contributed equally.

Notes

†We note that in our previous works,[8,10] $\Gamma_{HA\text{-}\beta\text{-}CD}$ referred to the amount of polymer that remains stably bound after buffer rinsing.

ACKNOWLEDGMENT

This work was supported by the Marie Curie Career Integration Grant "CELLMULTIVINT" (PCIG09-GA-2011-293803) to G.V.D, the European Research Council Starting Grant "JELLY," (306435) to R.P.R, Herchel Smith Scholarship to T.C, and the European Union's Horizon 2020 programme under ETN grant 674979-NANOTRANS and EPSRC to D.F. We are grateful to L. Yate (CIC biomaGUNE) for providing metal surface coatings, and R. Auzely-Velty (CERMAV, Grenoble, France) for support with HA conjugation.

REFERENCES

(1) Mammen, M.; Choi, S.-K.; Whitesides, G. M. Polyvalent Interactions in Biological Systems: Implications for Design and Use of Multivalent Ligands and Inhibitors. *Angew. Chem. Int. Ed.* **1998**, *37* (20), 2754–2794.
(2) Fasting, C.; Schalley, C. A.; Weber, M.; Seitz, O.; Hecht, S.; Koksch, B.; Dernedde, J.; Graf, C.; Knapp, E.-W.; Haag, R. Multivalency as a Chemical Organization and Action Principle. *Angew. Chem. Int. Ed Engl.* **2012**, *51* (42), 10472–10498.
(3) Kiessling, L. L.; Lamanna, A. C. Multivalency in Biological Systems. *SpringerLink* **2003**, 345–357.
(4) Varner, C. T.; Rosen, T.; Martin, J. T.; Kane, R. S. Recent Advances in Engineering Polyvalent Biological Interactions. *Biomacromolecules* **2015**, *16* (1), 43–55.
(5) van der Meulen, S. A. J.; Leunissen, M. E. Solid Colloids with Surface-Mobile DNA Linkers. *J. Am. Chem. Soc.* **2013**, *135* (40), 15129–15134.
(6) Ling, X. Y.; Reinhoudt, D. N.; Huskens, J. Reversible Attachment of Nanostructures at Molecular Printboards through Supramolecular Glue. *Chem. Mater.* **2008**, *20* (11), 3574–3578.
(7) Dubacheva, G. V.; Galibert, M.; Coche-Guerente, L.; Dumy, P.; Boturyn, D.; Labbé, P. Redox Strategy for Reversible Attachment of Biomolecules Using Bifunctional Linkers. *Chem Commun* **2011**, *47* (12), 3565–3567.
(8) Dubacheva, G. V.; Curk, T.; Mognetti, B. M.; Auzély-Velty, R.; Frenkel, D.; Richter, R. P. Superselective Targeting Using Multivalent Polymers. *J. Am. Chem. Soc.* **2014**, *136* (5), 1722–1725.
(9) Martinez-Veracoechea, F. J.; Frenkel, D. Designing Super Selectivity in Multivalent Nano-Particle Binding. *Proc. Natl. Acad. Sci.* **2011**, *108* (27), 10963–10968.
(10) Dubacheva, G. V.; Curk, T.; Auzély-Velty, R.; Frenkel, D.; Richter, R. P. Designing Multivalent Probes for Tunable Superselective Targeting. *Proc. Natl. Acad. Sci.* **2015**, *112* (18), 5579–5584..
(11) Wolny, P. M.; Banerji, S.; Gounou, C.; Brisson, A. R.; Day, A. J.; Jackson, D. G.; Richter, R. P. Analysis of CD44-Hyaluronan Interactions in an Artificial Membrane System: Insights into the Distinct Binding Properties of High and Low Molecular Weight Hyaluronan. *J. Biol. Chem.* **2010**, *285* (39), 30170–30180.
(12) Deeg, J.; Axmann, M.; Matic, J.; Liapis, A.; Depoil, D.; Afrose, J.; Curado, S.; Dustin, M. L.; Spatz, J. P. T Cell Activation Is Determined by the Number of Presented Antigens. *Nano Lett.* **2013**, *13* (11), 5619–5626.
(13) Cavalcanti-Adam, E. A.; Volberg, T.; Micoulet, A.; Kessler, H.; Geiger, B.; Spatz, J. P. Cell Spreading and Focal Adhesion Dynamics Are Regulated by Spacing of Integrin Ligands. *Biophys. J.* **2007**, *92* (8), 2964–2974.
(14) Elias, D. R.; Poloukhtine, A.; Popik, V.; Tsourkas, A. Effect of Ligand Density, Receptor Density, and Nanoparticle Size on Cell Targeting. *Nanomedicine Nanotechnol. Biol. Med.* **2013**, *9* (2), 194–201.
(15) Kiessling, L. L.; Gestwicki, J. E.; Strong, L. E. Synthetic Multivalent Ligands as Probes of Signal Transduction. *Angew. Chem. Int. Ed Engl.* **2006**, *45* (15), 2348–2368.
(16) Rai, P.; Padala, C.; Poon, V.; Saraph, A.; Basha, S.; Kate, S.; Tao, K.; Mogridge, J.; Kane, R. Statistical Pattern Matching Facilitates the Design of Polyvalent Inhibitors of Anthrax and Cholera Toxins. *Nat Biotech* **2006**, *24* (5), 582–586.
(17) Ravoo, B. J.; Jacquier, J.-C.; Wenz, G. Molecular Recognition of Polymers by Cyclodextrin Vesicles. *Angew. Chem. Int. Ed.* **2003**, *42* (18), 2066–2070.
(18) Nicolson, G. L. The Fluid—Mosaic Model of Membrane Structure: Still Relevant to Understanding the Structure, Function and Dynamics of Biological Membranes after More than 40 Years. *Biochim. Biophys. Acta BBA - Biomembr.* **2014**, *1838* (6), 1451–1466.
(19) Hartman, N. C.; Groves, J. T. Signaling Clusters in the Cell Membrane. *Curr. Opin. Cell Biol.* **2011**, *23* (4), 370–376.
(20) Yap, A. S.; Brieher, W. M.; Pruschy, M.; Gumbiner, B. M. Lateral

Clustering of the Adhesive Ectodomain: A Fundamental Determinant of Cadherin Function. *Curr. Biol.* **1997**, *7* (5), 308–315.
(21) Besschetnova, T. Y.; Montefusco, D. J.; Asinas, A. E.; Shrout, A. L.; Antommattei, F. M.; Weis, R. M. Receptor Density Balances Signal Stimulation and Attenuation in Membrane-Assembled Complexes of Bacterial Chemotaxis Signaling Proteins. *Proc. Natl. Acad. Sci.* **2008**, *105* (34), 12289–12294.
(22) Briegel, A.; Li, X.; Bilwes, A. M.; Hughes, K. T.; Jensen, G. J.; Crane, B. R. Bacterial Chemoreceptor Arrays Are Hexagonally Packed Trimers of Receptor Dimers Networked by Rings of Kinase and Coupling Proteins. *Proc. Natl. Acad. Sci.* **2012**, *109* (10), 3766–3771.
(23) Pfeiffer, A.; Böttcher, A.; Orsó, E.; Kapinsky, M.; Nagy, P.; Bodnár, A.; Spreitzer, I.; Liebisch, G.; Drobnik, W.; Gempel, K.; et al. Lipopolysaccharide and Ceramide Docking to CD14 Provokes Ligand-Specific Receptor Clustering in Rafts. *Eur. J. Immunol.* **2001**, *31* (11), 3153–3164.
(24) Bunnell, S. C.; Hong, D. I.; Kardon, J. R.; Yamazaki, T.; McGlade, C. J.; Barr, V. A.; Samelson, L. E. T Cell Receptor Ligation Induces the Formation of Dynamically Regulated Signaling Assemblies. *J. Cell Biol.* **2002**, *158* (7), 1263–1275.
(25) Sieber, J. J.; Willig, K. I.; Kutzner, C.; Gerding-Reimers, C.; Harke, B.; Donnert, G.; Rammner, B.; Eggeling, C.; Hell, S. W.; Grubmüller, H.; et al. Anatomy and Dynamics of a Supramolecular Membrane Protein Cluster. *Science* **2007**, *317* (5841), 1072–1076.
(26) Tzlil, S.; Ben-Shaul, A. Flexible Charged Macromolecules on Mixed Fluid Lipid Membranes: Theory and Monte Carlo Simulations. *Biophys. J.* **2005**, *89* (5), 2972–2987.
(27) Martinez-Veracoechea, F. J.; Leunissen, M. E. The Entropic Impact of Tethering, Multivalency and Dynamic Recruitment in Systems with Specific Binding Groups. *Soft Matter* **2013**, *9* (12), 3213–3219.
(28) Curk, T.; Dobnikar, J.; Frenkel, D. Design Principles for Super Selectivity Using Multivalent Interactions. In *Multivalency: Concepts, Research and Applications*; J. Huskens et al., 2018; pp 75–102.
(29) Grochmal, A.; Ferrero, E.; Milanesi, L.; Tomas, S. Modulation of In-Membrane Receptor Clustering upon Binding of Multivalent Ligands. *J. Am. Chem. Soc.* **2013**, *135* (27), 10172–10177.
(30) Dubacheva, G. V.; Araya-Callis, C.; Geert Volbeda, A.; Fairhead, M.; Codée, J.; Howarth, M.; Richter, R. P. Controlling Multivalent Binding through Surface Chemistry: Model Study on Streptavidin. *J. Am. Chem. Soc.* **2017**, *139* (11), 4157–4167.
(31) Burdick, J. A.; Prestwich, G. D. Hyaluronic Acid Hydrogels for Biomedical Applications. *Adv. Mater. Deerfield Beach Fla* **2011**, *23* (12), H41-56.
(32) Toole, B. P. Hyaluronan: From Extracellular Glue to Pericellular Cue. *Nat. Rev. Cancer* **2004**, *4* (7), nrc1391. https://doi.org/10.1038/nrc1391.
(33) Morra, M. Engineering of Biomaterials Surfaces by Hyaluronan. *Biomacromolecules* **2005**, *6* (3), 1205–1223.
(34) Migliorini, E.; Thakar, D.; Kühnle, J.; Sadir, R.; Dyer, D. P.; Li, Y.; Sun, C.; Volkman, B. F.; Handel, T. M.; Coche-Guerente, L.; et al. Cytokines and Growth Factors Cross-Link Heparan Sulfate. *Open Biol.* **2015**, *5* (8).
(35) Kühnle, J. Lipid Assemblies on Nanostructured Surfaces. Diploma thesis, Faculty of Physics and Astronomy, University of Heidelberg, 2007.
(36) Richter, R. P.; Rodenhausen, K. B.; Eisele, N. B.; Schubert, M. Coupling Spectroscopic Ellipsometry and Quartz Crystal Microbalance to Study Organic Films at the Solid-Liquid Interface. In *Ellipsometry of Functional Organic Surfaces and Films*; Hinrichts, K., Eichhorn, K.-J., Eds.; Springer Series in Surface Sciences; Springer: Berlin, Heidelberg, 2014; Vol. 52, pp 223–238.
(37) Takahashi, R.; Kubota, K.; Kawada, M.; Okamoto, A. Effect of Molecular Weight Distribution on the Solution Properties of Sodium Hyaluronate in 0.2M NaCl Solution. *Biopolymers* **1999**, *50* (1), 87–98.
(38) Ringsdorf, H.; Schlarb, B.; Venzmer, J. Molecular Architecture and Function of Polymeric Oriented Systems: Models for the Study of Organization, Surface Recognition, and Dynamics of Biomembranes. *Angew. Chem. Int. Ed. Engl.* **1988**, *27* (1), 113–158.
(39) Ringsdorf, H.; Venzmer, J.; Winnik, F. M. Interaction of Hydrophobically-Modified Poly-N-Isopropylacrylamides with Model Membranes—or Playing a Molecular Accordion. *Angew. Chem. Int. Ed. Engl.* **1991**, *30* (3), 315–318.
(40) Holzinger, M.; Singh, M.; Cosnier, S. Biotin−β-Cyclodextrin: A New Host–Guest System for the Immobilization of Biomolecules. *Langmuir* **2012**, *28* (34), 12569–12574.
(41) Roling, O.; Wendeln, C.; Kauscher, U.; Seelheim, P.; Galla, H.-J.; Ravoo, B. J. Layer-by-Layer Deposition of Vesicles Mediated by Supramolecular Interactions. *Langmuir* **2013**, *29* (32), 10174–10182.
(42) Lee, H.; Venable, R.; MacKerell, A.; Pastor, R. W. Molecular Dynamics Studies of Polyethylene Oxide and Polyethylene Glycol: Hydrodynamic Radius and Shape Anisotropy. *Biophys J* **2008**, *95* (4), 1590–1599.
(43) Curk, T.; Dobnikar, J.; Frenkel, D. Optimal Multivalent Targeting of Membranes with Many Distinct Receptors. *Proc Natl Acad Sci USA* **2018**, *114* (28), 7210–7215.
(44) Freeman, S. A.; Vega, A.; Riedl, M.; Collins, R. F.; Ostrowski, P. P.; Woods, E. C.; Bertozzi, C. R.; Tammi, M. I.; Lidke, D. S.; Johnson, P.; et al. Transmembrane Pickets Connect Cyto- and Pericellular Skeletons Forming Barriers to Receptor Engagement. *Cell* **2018**, *172* (1), 305-317.e10.

TOC figure

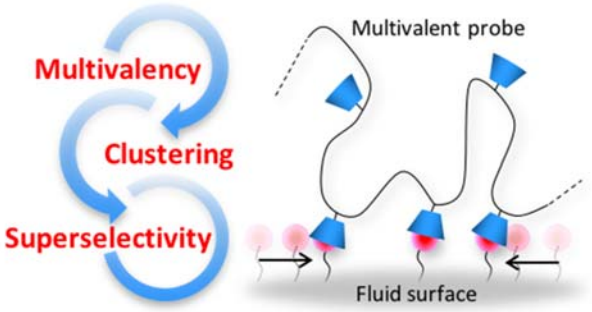
Multivalency
Clustering
Superselectivity
Multivalent probe
Fluid surface